Stimulated Emission Imaging

View On GitHub

Download PDF

This project is maintained by Sanjay R. Varma in the York lab, and was funded by Calico Life Sciences LLC

Appendix

Note that this is a limited PDF or print version; animated and interactive figures are disabled. For the full version of this article, please visit one of the following links:
https://andrewgyork.github.io/stimulated_emission_imaging
https://calico.github.io/stimulated_emission_imaging

Stimulated Emission Imaging

Back to the main text

Rate constants for fluorophores

In [Hell 1994], the spontaneous emission rate constant of the excited state of a fluorophore is $1/\tau_{fluor}$, and Q is the nonradiative quenching rate of the excited state. The combined rate constant $1/\tau_{exc} = 1/\tau_{fluor} + Q$ is the inverse of the excited state lifetime, which is commonly called the fluorescence lifetime when it is measured. The quantum yield Φ is the ratio between the spontaneous emission rate constant and the total excited state decay rate constant: $\Phi = \tau_{exc}/\tau_{fluor}$.

In the introduction to the main article, we cite GFP and Alexa Fluor 488 dye as examples to highlight the difference between the magnitude of the spontaneous emission rate constant $1/\tau_{fluor}$ and the intensity-dependent stimulated emission rate constant. The reference for those rates only specifies the more easily measured τ_{exc} (3.2 ns for GFP and 4.0 ns for Alexa 488) [Berezin 2010]. We compute τ_{fluor} by first looking up Φ for both fluorophores (0.79 for GFP [Patterson 1997] and 0.92 for Alexa 488 [Johnson 2010]) and then using the measured τ_{exc} as well as the relationship in the previous paragraph to arrive at τ_{fluor} of 4.1 ns for GFP and 4.3 ns for Alexa 488.

Nanodiamond properties and mounting

Diamond samples doped with nitrogen-vacancy (N-v) centers absorb green light, emit bright red fluorescence, and do not photobleach [Gruber 1997]. Figure A1 is a sample transmission electron microscope image (TEM) of nanodiamonds like the ones we imaged. The TEM image and cover glasses with mounted nanodiamonds were a kind gift from Keir Neuman (National Heart, Lung and Blood Institute, National Institute of Health, Bethesda, MD). The nanodiamonds have an average diameter of ~80 nm, but vary widely in shape and size. The nanodiamonds were spun down for 1 minute at 10,000 rpm in a benchtop centrifuge to remove large aggregates. The supernatant was collected and mixed in 1:10 proportion with poly-lysine (Sigma-Aldrich). 20 µl of the mixture was then deposited on a cover glass rotating at 12,000 rpm in a spin coater (Laurell Technologies). We put a drop of immersion oil (Nikon Type A, n = 1.515) on the nanodiamond side of the cover glass and sandwiched it between the cover glass and a 1 mm thick BK7 or fused silica glass window. The circular sample is then put into the sample holder and imaged.

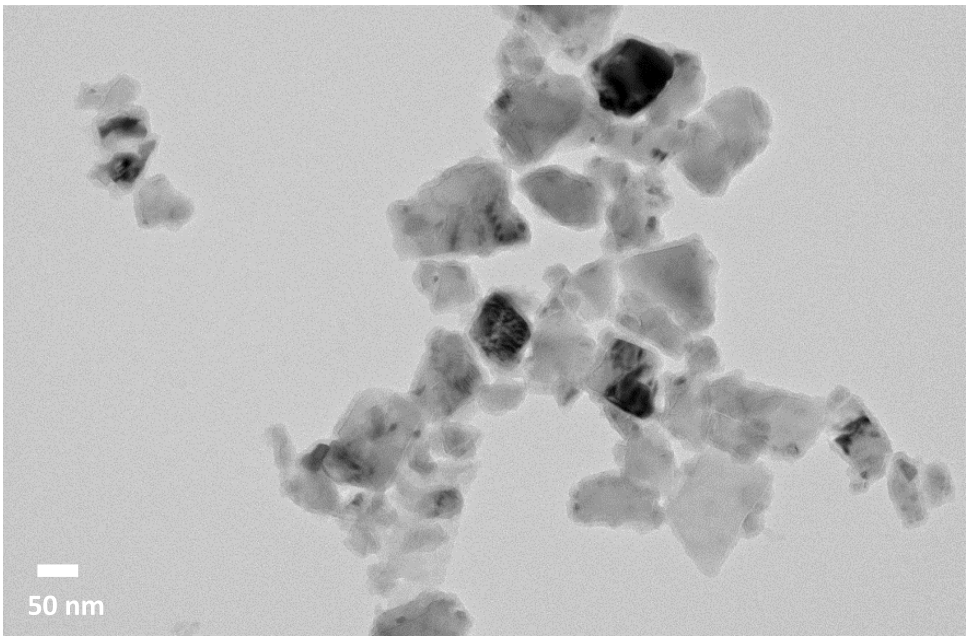

Figure A1: TEM image of a cluster of nanodiamonds doped with N-v centers. Scale bar: 50 nm.

Fluorescent polystyrene bead properties and mounting

We bought the 200 nm diameter crimson and orange fluorescent dyed polystyrene beads in a 2% solid solution. We display excitation and emission spectra in Figure 2b in the main article with `Fluorescent sample type: Beads...` selected. In later sections of this appendix, we show how we measured the fluorescence lifetime and the quantum yield of the beads.

To prepare the beads, we first cleaned a 1" diameter cover glass with de-ionized water and then applied a 200 µL drop of poly-L-lysine solution (Electron Microscopy Sciences) to the center. After ten minutes, we removed as much of the poly-L-lysine as possible with a pipette, leaving an invisibly thin layer. We then washed off excess poly-L-lysine by applying 200 µL de-ionized water to the center of the cover glass and immediately removing it. We then further diluted the bead solution by 3 parts in 10^6 with de-ionized water and added 100 µL of the diluted bead solution to the center of the cover glass. We allowed the solution to remain on the cover glass for 20 minutes and then removed it with the pipette.

We prepared the beads (polystyrene refractive index n ≈ 1.6) in mounting media with three distinct refractive indices greater than, equal to, and less than 1.6 (as explained in the main article, we used these media in order to estimate the relative phase between transmitted, scattered, and stimulated light). We used commercially available mounting media with refractive index 1.539, 1.582 and 1.605. For index-matched beads, we made a 1:1 mixture of the n = 1.582 and n = 1.605 mounting media in a glass beaker on a hot plate and dropped it onto a 1 mm thick, 1" diameter BK7 or fused silica glass window. We then carefully pressed the cover glass (bead side down) onto the glass window and allowed it to cool. The circular sample is then put into the sample holder and imaged. The 1:1 ratio made the scatter from the beads least visible in our phase contrast microscope. We therefore estimated the refractive index of the beads to be ~ 1.594. We additionally mounted the beads in only n = 1.539 media (Δn ~ 0.05) and n = 1.605 media (Δn ~ -0.01).

Fluorescence lifetime measurements

We measure the excited state lifetime (τ_{exc}) of the crimson and orange dyed polystyrene beads, as well as the N-v center doped nanodiamonds, using the fluorescence lifetime imaging (FLIM) module of a Leica SP8 confocal microscope. Excitation wavelengths were 561 nm (orange beads and nanodiamonds) and 594 nm (crimson beads), as opposed to 532 nm; these were chosen because they matched the emission filters that better shield the FLIM module from excitation light. The lifetime curves of the crimson and orange beads were well-fit by a single exponential function, yielding lifetimes of 2.89 ± 0.05 ns (crimson beads) and 3.85 ± 0.03 ns

(orange beads). The N-v doped nanodiamonds yielded lifetime curves that could not be fit by a single exponential because of a small fast-decaying signal, but a two-exponential fit yielded a primary lifetime of 12.41 ± 0.13 ns, and a secondary lifetime of 1.135 ± 0.041 ns. The ~12 ns lifetime seemingly agrees with measurements of the excited state lifetime of N-v centers in bulk diamond [Doherty 2013], though single N-v centers in nanodiamonds with diameter less than the wavelength of fluorescent emission has been measured to be 25 ns, with the discrepancy attributed to the large difference in refractive index between the nanodiamond and its surroundings [Beveratos 2001].

Sample holder and vibration isolation

Imaging stimulated emission via our experimental setup involves using our camera to resolve signals of ~10-100 pixel counts on top of a background of ~20,000-50,000 pixel counts. Because the laser power fluctuations can exceed the signal level, averaging of images is important to be able to observe the signal. However, vibration of the sample makes averaging separate images difficult. In order to combat vibration, we attempted to mount our samples as stably as possible. We secured our 1" diameter circular samples in a lens mount and anchored it to a 3D stage comprised of a manual vertical stage, a manual horizontal stage, and an axial stage fitted with a piezoelectric actuator to take automated axial stacks of the sample.

The entire microscope is screwed onto a floating optical table for vibrational isolation from the floor. The 532 nm laser has an on-board fan that caused vibration of the sample through the optical table. In order to solve this problem, we detached the fan from the back of the laser head and anchored it to a nearby wall not in contact with the optical table. We connected the back of the laser head to the fan with a thin polyethylene bellows, which allowed the fan to continue to pull air from the laser.

Parts list

Supplier	Part	Description
Cargille Labs	24040	Meltmount™ Quick-Stick™ mounting medium, n = 1.539
Cargille Labs	24050	Meltmount™ Quick-Stick™ mounting medium, n = 1.582
Cargille Labs	24052	Meltmount™ Quick-Stick™ mounting medium, n = 1.605
Chroma	ZT532rdc	Dichroic beamsplitter to used to combine 532 nm (45° reflected) and 721 nm (transmitted) laser beams
Chroma	ZET532NF	Notch filter to block 532 nm excitation light after sample illumination
Chroma	ET720/10m	10 nm narrow bandpass filter centered at 720 nm to block fluorescence and pass stimulated emission
Chroma	ET680sp-2P8	Shortpass filter to block stimulated emission and allow fluorescence
Gooch & Housego	AOMO 3200-125	Visible wavelength acousto-optic modulator crystal (one for the 532 nm laser and one for the 721 nm laser). RF supplied by green and red AOM drivers.
Gooch & Housego	1080AF-AINA-1.0 HCR	Analog RF driver for 532 nm laser acousto-optic modulator. Triggered by analog out card with a buffer amplifier for higher current.
Gooch & Housego	1080AF-AINA-2.5 HCR	Analog RF driver for 721 nm laser acousto-optic modulator. Triggered by analog out card with a buffer amplifier for higher current.
Leica	HCX PL APO 100x/1.40-0.70 OIL	100X plan apo NA = 1.4 objective used for imaging
Molecular Devices	SpectraMax i3x	Multi-mode microplate reader used to measure fluorescence and absorbance
Mitutoyo	Edmund optics part	10X plan apo infinity corrected long working distance objective used for sample illumination

	#46-144	
National Instruments	NI PCI-6733	Analog output board to trigger the camera and AOMs. BNC connector block interface.
National Instruments	BNC-2110	Connector block to interface with analog output board
Newport	M-RS4000-46-12	1200 x 1800 x 305 mm optical table floating on four legs
Newport	S-2000	Air-powered legs (4) to support the optical table
Opto-Engine	MLL-F-532-2.5W	2.5 Watt CW laser with 532 nm wavelength
Opto-Engine	MRL-FN-721-300mW	0.3 Watt CW laser with 721 nm wavelength
PCO	edge4.2.WAT	PCO.edge 4.2 water-cooled rolling shutter sCMOS camera. Triggered by analog output board.
Photo Sciences Inc.	custom (website)	512 µm diameter, OD5 chrome disc plated on 2.38 mm thick glass plate. Discs with other diameters are plated nearby on the same substrate.
Photo Sciences Inc.	custom (website)	512 µm outer diameter, 9 µm inner diameter, OD5 chrome annulus plated on 2.38 mm thick glass plate. Annuli with different inner and outer diameters are plated nearby on the same substrate. (The annulus we used passes a small fraction of the transmitted beam, which diverges more strongly due to the 9 µm hole. The net effect is ~150-fold attenuation of the coherent background intensity.)
Potomac Photonics	custom (website)	0.18 mm thick cover glass with a 90 µm diameter hole drilled by laser (the "phase plate" in Figure 2)
San Mateo Electronics	LM324N	Operational amplifiers (set up as buffer amplifiers) to supply amplified current to AOM drivers from analog out board. Voltage stabilized by 24 Volt regulator
San Mateo Electronics	LM7824	24V regulator for buffer amps
Thermo Fisher	F8806	200 nm diameter polystyrene beads labeled with crimson fluorescent dye
Thermo Fisher	F8809	200 nm diameter polystyrene beads labeled with orange fluorescent dye
Thorlabs	PE4	Piezoelectric actuator to position sample axially. Controlled by piezo controller.
Thorlabs	MDT694B	Serial port-driven controller for Thorlabs piezoelectric actuator.
Thorlabs	FESH0700	Shortpass filter to block stimulated emission and allow fluorescence
Thorlabs	FELH0600	Longpass filter to block excitation and allow stimulated emission and fluorescence
Thorlabs	FBH520-40	Bandpass filter used to remove IR from 532 nm laser beam
Thorlabs	FELH0700	Longpass filter used to remove visible light from 721 nm laser beam
Thorlabs	BB1-E02	Broadband dielectric mirrors
Thorlabs	AC254-100-B-ML	100 mm focal length tube lens following Leica 100X imaging objective lens
Thorlabs	AC254-040-B-ML	40 mm focal length lens following Thorlabs 100mm tube lens and before phase plate
Thorlabs	AC254-100-A-ML	100 mm focal length lens following phase plate
Thorlabs	AC254-050-B-ML	50 mm focal length lens following 100 mm focal length lens and before chrome mask
Thorlabs	AC254-300-	300 mm focal length lens following chrome mask and before camera

	A-ML	
Thorlabs	TRH127-020-A-ML	20 mm focal length lens immediately after 532 nm laser to collimate beam
Thorlabs	AHWP05M-600	Achromatic half wave plates used to tune polarization of 532 nm and 721 nm lasers
Thorlabs	GT10-A	Glan Taylor calcite polarizer visible anti-reflection coated to clean up 532 nm laser polarization prior to AOM
Thorlabs	GT10-B	Glan Taylor calcite polarizer near-IR anti-reflection coated to clean up 721 nm laser polarization prior to AOM
Thorlabs	LMR1/M	Lens mount used to hold nanodiamonds or beads mounted in between 1" diameter pieces of glass
Thorlabs	MVS005/M	13 mm travel manual vertical translation stage for sample
Thorlabs	MT1/M	13 mm travel manual horizontal translation stage for sample
Thorlabs	PT1/M	25 mm translation stage fitted with a piezoelectric actuator to the sample axially for automated z stack acquisition
various	ET720/10m, FELH0600	Filter set used to block fluorescence and pass stimulated emission
various	ET680sp-2P8, FESH0700, FELH0600	Filter set used to block stimulated emission and pass fluorescence

Image acquisition and figure generation

For every experiment we do that contributes to a figure, we store a copy of the python code used to control and synchronize our instruments, along with code dependencies, in the data acquisition folder. These files generated many raw camera images, which we have made available in dedicated repositories for the main article data (https://doi.org/10.5281/zenodo.3659378) and the appendix data (https://doi.org/10.5281/zenodo.3659380). In some cases, the repositories will also store repetition-averaged images (in order to decrease run-time of our figure generation code).

Each figure that contains experimental data is generated by a python script bearing the same name as the figure that can be found in the figure generation folder. These scripts refer to the appropriate images from the downloaded data repository, process the images appropriately (phase contrast and dark-field image processing), generate figures, and then store those figures in `.svg` or `.png` format in the images directory.

Phase contrast image generation

Phase contrast image acquisition details

We illuminate fluorescent samples comprised of dyed beads or nanodiamonds with a train of several green excitation (532 nm) laser pulses as well as several pulses of red (721 nm) light in order to stimulate emission from the samples, and we use part of the stimulation beam as a coherent background in order to generate a phase contrast image of the stimulated emission (see Figure 2b in the main article with `Imaging method: Phase contrast imaging of stimulated emission and scattered light` selected). The red pulses are 1.25 μs in duration and are separated by 600 μs. The green pulses are also 1.25 μs in duration and are separated by 600 μs. Because it is not obvious which phase plate angle will provide the best relative background phase shift to detect the emission from the sample, we take phase contrast images of the sample for a variety of phase plate angles. For each phase plate angle, a typical measurement involves three sequential camera exposures (example code):

1. During the first exposure, the red pulse train precedes the green pulse train by 2.5 μs. Because 600 μs is much longer than the excitation lifetime, there should be no stimulated emission.
2. During the second exposure, the red and green pulses are simultaneous. Stimulated emission should be possible.
3. During the third exposure, the green pulse train precedes the red pulse train by 2.5 μs. Because 2.5 μs is much longer than the excitation lifetime, there should be no stimulated emission. If the green pulse modifies the sample in a time-delayed fashion (e.g. heating) and this effect persists longer than 2.5 μs, there may be some effect on the phase contrast image.

Phase contrast difference image processing

The difference between the first and second exposure (of the three listed above) should let us know the effect of excitation on the phase contrast image of the beam. However, simply subtracting one image from the other is not sufficient; the red laser intensity fluctuates between those two exposures. In our image extraction code (example), we re-scale the two images prior to subtraction in this manner:

1. We estimate the average brightness of the red laser by averaging all phase contrast images and then finding the mean pixel value of the regions of the image that do not contain the sample particle (the background).
2. We estimate the brightness of the red laser in each exposure by finding the mean pixel value of the background of each exposure.
3. We re-scale each individual exposure by a factor of the ratio of the average background to its own background.

After re-scaling all of the phase contrast images, we then subtract the first exposure from the second exposure, resulting in a "difference image" that encapsulates the effect of excitation on the phase contrast image. While we use 750x total magnification (8.7 nm/pixel) to give large dynamic range, this is not great for viewing our difference images, because intra-pixel fluctuations can appear to swamp the signal. Prior to display of the difference images, we bin 8 x 8 regions of pixels to give a more typical size (69.6 nm/pixel).

Figure A2 shows a sample phase contrast image of an index-matched crimson bead prior to excitation, and the change in that image during and after excitation, based upon the experimental method and image processing steps delineated above. The phase plate angle is tuned to maximize contrast of the difference image. For each exposure, we used 8 maximum-intensity excitation/stimulation pulse pairs with 1.25 μs duration and 600 μs between pairs.

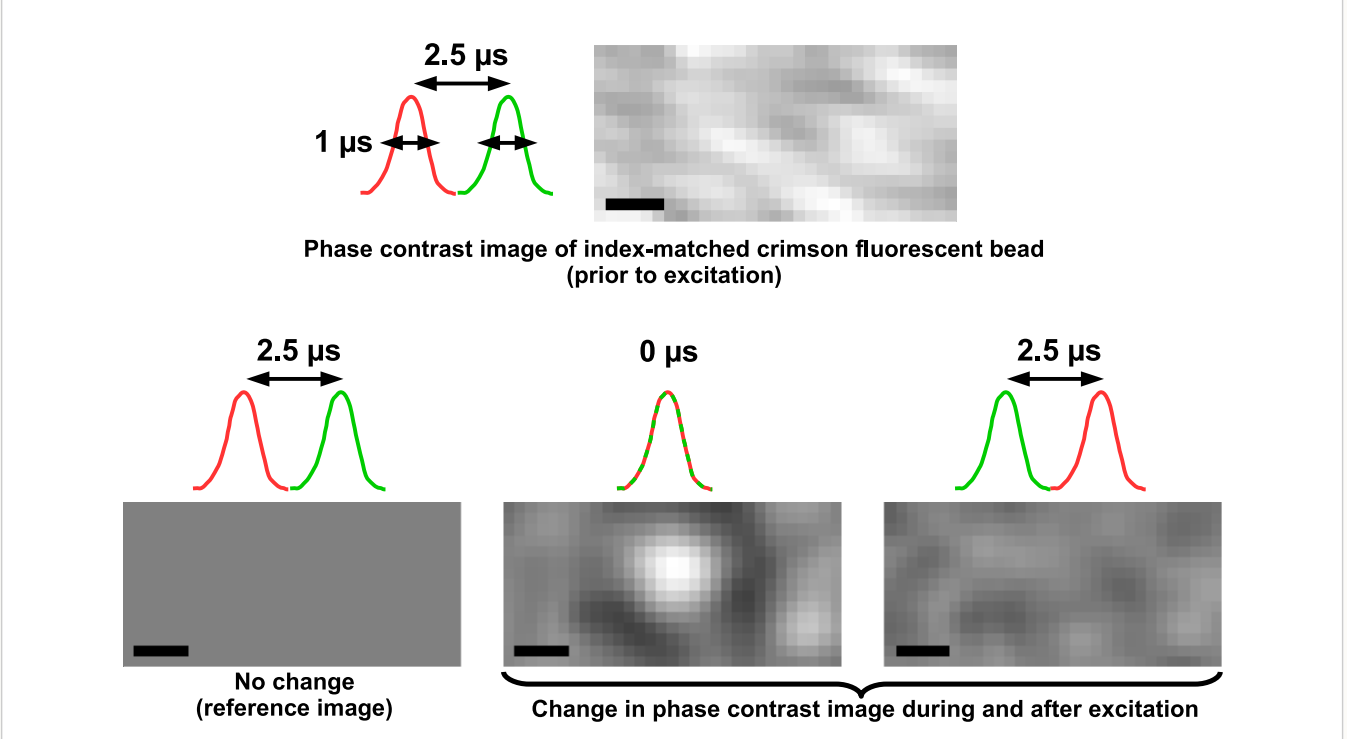

Figure A2: The change in the phase contrast bead image due to excitation has a sub-microsecond response time. Scanning the delay between the excitation (green) and stimulation (red) laser pulses shows the observed change in the phase contrast signal from a crimson bead has a timescale at least as short as the laser pulse duration (1.25 µs). Scale bar: 350 nm.

Extra processing for phase contrast imaging of weakly scattered light

While the above processing is all that is involved in generating the stimulated emission "difference images," making simple phase contrast images of scattered light from the polystyrene beads requires a few more steps. This is because there is a large, spatially inhomogeneous background variation in the simple phase contrast images due to multiple reflections in the microscope. Some of the background features appear to vary in location and brightness only when the phase plate moves (the "stationary component"), and some features vary regardless of whether the phase plate has changed (the "non-stationary component"). The difference images are taken at a single particular phase plate angle, so they are only subject to non-stationary noise. Luckily, the non-stationary background inhomogeneities appear to vary more slowly than the camera exposure rate, so the difference images, which are the difference between adjacent exposures, are not adversely affected (this is akin to lock-in detection). On the other hand, because the beads are either fairly or extremely well index-matched to their mounting media, their static scattering is nearly or completely invisible atop the stationary and non-stationary background variations, and we cannot switch scattering on and off quickly enough to elude those variations.

After performing overall brightness correction on the simple phase contrast bead images, we attempt to remove the stationary component from each bead image with another phase contrast image at a nearby phase plate angle at which the scattered light contrast would be minimal (least amount of constructive or destructive interference). We then note that the remaining stationary and non-stationary and components of the background noise in the phase contrast images are primarily comprised of stripes—presumably an interference pattern from multiple coherent reflections—that are completely outside of the microscope's spatial pass-band. We perform a gaussian filter on the phase contrast images to attenuate the high-frequency artifacts with almost no effect on the spatial frequencies due to the sample.

We finally bin the phase contrast image pixels in the same manner as we did for the difference images. By performing these additional steps, we find it possible to image light scattered from nearly perfectly index-matched beads $(\Delta n \approx -0.01)$, as seen in Figure 3 (top right panel) in the main article.

Fitting to the photobleaching curve

We performed the experiment in Figure 4 of the main text in order to confirm that, like fluorescence, our phase contrast difference images of excited beads faded during prolonged exposure to excitation power. Although we did, indeed, find that the difference images and fluorescence images of both crimson and orange beads faded, we also found it difficult to quantify and compare the bleaching rates. A single exponential function did not fit any of the bleaching curves we acquired. Rather, we were only able to get a good fit of the fluorescence bleaching curves with a 4-exponential fit—for beads that were only excited, and for beads that were excited and depleted.

In fact, many fluorophores do not have a single (mono-exponential) bleaching rate, including fluorescent dyes like Rhodamine 6G [Zondervan 2004] and the Alexa Fluor family [Panchuk-Voloshina 1999], as well as genetically-expressed fluorophores like GFP and its variants [Patterson 1997]. As with our beads, all of the dyes measured by Panchuk-Voloshina et al. exhibit fast initial brightness decay followed by more gradual decay, regardless of mounting medium type (although the absolute bleaching rates were strongly affected by the mounting medium) [Panchuk-Voloshina 1999]. Zondervan et al. also observed that Rhodamine 6G bleaching curves exhibited "strong deviation" from single exponential fits, and suggested an ensemble bleaching model comprised of multiple bleaching rates from both emissive and dark excited states of the fluorophores [Zondervan 2004]. Additionally, our use of linearly polarized excitation for fluorophores with random orientation could be another source of multi-exponential fluorescence bleaching. All told, we believe that the complicated bleaching rates we measured are not unusual. The most we can conclude from our measurements is that bead fluorescence and difference images co-decrease; in order to tell if one truly affects the other, we need a dual-camera setup (or at least a fast filter wheel) to monitor fluorescence and difference image decay from the same bead.

Delivering the same heat load to the orange beads

Our experimentally generated difference images of excited fluorescent crimson beads in Figures 3 and 4 in the main article are consistent with the model proposed in Figure 1c: that stimulated emission emits spherically from a point source and can by imaged via interference with the stimulating beam. However, these results may also be consistent with a model where the excitation pulse heats the bead and causes its refractive index to change. In order to discern between the two models, we additionaly performed phase contrast imaging of excited orange dyed polystyrene beads, which have a lower stimulated emission cross-section than crimson beads at 721 nm; this allowed us to decrease the expected amount of stimulated emission from a bead while delivering the same thermal energy. We expect that if our difference images are stimulated emission images, the orange bead difference images should be dimmer than the crimson bead images. If our difference images are photothermal images, the difference images of the different beads should have the same brightness.

In order to deliver the same thermal energy to the orange beads as we did to the crimson beads in earlier experiments through excitation at 532 nm wavelength, we had to carefully account for the fact that orange beads have a different fluorescent efficiency and excitation cross-section than crimson beads.

We first measured the fluorescent efficiency η of both the crimson and orange dye using a fluorometer to measure fluorophore absorption and emission. Measuring absolute fluorescent efficiency is difficult, so we used Rhodamine B as a reference standard. The Rhodamine B quantum yield $\Phi = 0.49$ in ethanol at room temperature [Casey 1988], and $\eta = \Phi \frac{\lambda_{excitation}}{\overline{\lambda_{fluorescence}}}$, where $\lambda_{excitation}$ and $\overline{\lambda_{fluorescence}}$ are the excitation and average emission wavelengths. In this way, we measured $\eta_{crimson} = 0.17$ and $\eta_{orange} = 0.23$ for the beads suspended in TDE [Staudt 2007]; we did not have beads dyed with rhodamine.

We also fixed a mixture of crimson and orange beads in index-matched media on a microscope slide as described earlier and used a Leica SP8 confocal microscope to measure their total fluorescence under non-saturating 532 nm excitation (emission collection range set to 542-784 nm). Under identical excitation power, we measured a fluorescence brightness ratio $B_{orange}/B_{crimson} = 11.2$.

If E_{tot} is the total energy absorbed by a bead, and E_{opt} is the total optical energy emitted by a bead, then the fluorescent efficiency $\eta = E_{opt}/E_{tot}$. If the total energy absorbed by the bead is either optically emitted or transferred into heat energy H, then we can solve for H in terms of E_{opt}:

$$H = E_{tot} - E_{opt} = \frac{E_{opt}}{\eta} - E_{opt} = E_{opt}(\frac{1}{\eta} - 1)$$

The total emitted optical energy E_{opt} is proportional to bead brightness B, so:

$$H \propto B(\frac{1}{\eta} - 1)$$

We can finally solve for $H_{orange}/H_{crimson}$ at the same excitation power:

$$\frac{H_{orange}}{H_{crimson}} = \frac{B_{orange}(\frac{1}{\eta_{orange}} - 1)}{B_{crimson}(\frac{1}{\eta_{crimson}} - 1)} = 7.7$$

For the same excitation power, we estimate that orange beads will heat at a rate roughly eight times that of crimson beads. In order to heat orange beads at the same rate, we use one eighth of the crimson bead excitation power for our orange bead experiments, and keep all other acquisition parameters the same (Figure 4 and Figure 5 with `Fluorescent sample type: Bead labeled with orange dye` selected).

[Casey 1988] claims an uncertainty of 10% in their measured Φ for Rhodamine B. If this were the only source of error in our measurements, we would expect the uncertainty in our estimate of $H_{orange}/H_{crimson}$ to be 1%. If we propose an additional 5% uncertainty (2.5% standard deviation) to our measurements of $\eta_{crimson}$ and η_{orange}, as well as 10% uncertainty (5% standard

deviation) in our measurement of $B_{orange}/B_{crimson}$, we expect an uncertainty of 14% in our final estimate of $H_{orange}/H_{crimson}$. By choosing to excite the orange beads with 1/8 of the laser power that we used to excite the crimson beads, we estimate that we heated the two bead types fairly similarly.

In Figure 4 with `Imaging method: Phase contrast difference imaging of stimulated emission` selected, we observed a roughly 60% decrease in difference image signal magnitude when we changed from crimson to orange beads (prior to photobleaching). This confirms our expectation that a decrease in stimulated emission cross-section would decrease the difference image signal and that the signal is not likely thermally-induced refraction (the observed percent change is much greater than what we would expect from a thermal signal if we made any error in our estimation of the excitation power necessary to heat the crimson and orange beads identically).

As with the crimson beads, the orange bead's difference images fade over extended exposure to the excitation laser. The 9,000 difference images in Figure 4 exposed the orange bead to 216,000 130 mW excitation pulses. Under identical exposure parameters, the fluorescence images of another orange bead similarly fade (Figure 4 with `Imaging method: Fluorescence imaging` and `Fluorescent sample type: Bead labeled with orange dye` selected). The 15,000 fluorescence images in this panel exposed the orange bead to 360,000 130 mW excitation pulses. The orange bead difference image signal decreases more quickly than that from the crimson bead due to extended excitation, as one would predict from their differing fluorescence photobleaching rates.

Crimson bead excitation and emission rates

As discussed in [Hell 1994], the excited state population fraction n_2 depends on the excited state decay rate constant $1/\tau_{exc}$, the excitation and stimulated emission rate constants $h_{exc}\sigma_{01}$ and $h_{stim}\sigma_{23}$, as well as the vibrational relaxation rate constant $1/\tau_{vibr}$. In fluorophores, $1/\tau_{vibr}$ dominates $1/\tau_{exc}$, and given our modest laser intensities, it also dominates $h_{exc}\sigma_{01}$ and $h_{stim}\sigma_{23}$. In this limit, the model from [Hell 1994] reduces to:

$$\frac{dn_2}{dt} = h_{exc}\sigma_{01}(1 - n_2) - h_{stim}\sigma_{23}n_2 - \frac{1}{\tau_{exc}}n_2$$

More generally, excitation and stimulation rate constants depend on the angle θ between the fluorophore's transition dipole moments and the polarization of the illumination [Jameson 2010]. If we define σ_{01} and σ_{23} to be the cross-sections for fluorophores with transition dipole moments oriented parallel to the illumination polarization, and assume that the transition dipole moments for excitation and stimulated emission are parallel to each other, we can re-write this equation as a function of θ:

$$\frac{dn_2(\theta)}{dt} = h_{exc}\sigma_{01}\cos^2(\theta)(1 - n_2(\theta)) - h_{stim}\sigma_{23}\cos^2(\theta)n_2(\theta) - \frac{1}{\tau_{exc}}n_2(\theta)$$

where $n_2(\theta)$ is the excited state population fraction for molecules with orientation θ.

We'd like to confirm that our fluorescent signals are consistent with this model. We'd also like to estimate the relationships between fundamental quantities ($h_{exc}\sigma_{01}$, $h_{stim}\sigma_{23}$, and n_2) and measured quantities like P_{exc} (excitation power in milliwatts), P_{stim} (stimulation power in milliwatts), and C_{fluor} (fluorescent counts in camera digitizer units). Specifically, we want to estimate the ratio $R_{exc} = \frac{h_{exc}\sigma_{01}\tau_{exc}}{P_{exc}}$ between the normalized excitation rate constant and the measured excitation power, the ratio $R_{stim} = \frac{h_{stim}\sigma_{23}\tau_{exc}}{P_{stim}}$ between the normalized stimulation rate constant and the measured stimulation power, and the ratio $R_{fluor} = \frac{\overline{n_2}}{C_{fluor}}$ between the excited state population fraction $\overline{n_2}$ (averaged over fluorophore orientations) and the measured fluorescence.

We imaged a crimson bead from the same sample as the middle panels of Figure 3 with variable-power excitation pulses and full-power stimulation pulses. At each excitation power, we took three exposures with different stimulation pulse delays, yielding fluorescence images of beads excited 2.5 µs before stimulation, during stimulation, and 2.5 µs after stimulation. For each exposure, we used 8 excitation/stimulation pulse pairs with 1.25 µs pulse duration and 600 µs between consecutive pairs. In our results, we

observe that stimulation reduces fluorescence from the crimson beads (Figure 5 with `Fluorescent sample: Bead labeled with crimson dye` selected).

At steady state, $\frac{dn_2(\theta)}{dt} = 0$, which yields:

$$n_2(\theta) = \frac{h_{exc}\sigma_{01}\cos^2(\theta)}{h_{exc}\sigma_{01}\cos^2(\theta) + h_{stim}\sigma_{23}\cos^2(\theta) + \frac{1}{\tau_{exc}}}$$

We re-write this relationship in terms of our measured quantities C_{fluor}, P_{exc}, and P_{stim}:

$$\overline{n_2} = R_{fluor}C_{fluor} = \int_0^{2\pi}\int_0^{\pi} \frac{R_{exc}P_{exc}}{R_{exc}P_{exc} + R_{stim}P_{stim} + \frac{1}{cos^2(\theta)}}\psi(\phi,\theta)d\theta d\phi$$

where $\psi(\phi,\theta)$ is the normalized density of fluorophores versus orientation. We assume our beads contain a large number of randomly oriented fluorophores, giving $\psi(\phi,\theta) = \frac{\sin(\theta)}{4\pi}$. Note that randomly oriented fluorophores require much higher illumination intensity to saturate excitation, compared to fluorophores that are oriented parallel to the illumination polarization.

Our measurements are consistent with this model (Figure 5 with `Fit parameter` R_{fluor}`: Subjectively optimal` selected). Using $R_{fluor} = 6.94 \times 10^{-3}$ counts^{-1}, $R_{exc} = 2.04$ W^{-1}, and $R_{stim} = 1.33$ W^{-1} gives model predictions (green and red lines) that strongly resemble our experimental data (green and red dots). Neighboring values also produce reasonable fits. The green shaded area shows the range of the $P_{stim} = 0$ model (green line) as we vary R_{exc} by ± 7%. The red shaded area shows the range of the $P_{stim} \neq 0$ model (red line) as we vary R_{stim} by ± 40%. Grossly different values of R_{fluor} fit the data poorly for any value of R_{exc} and R_{stim} (Figure 5 with `Fit parameter` R_{fluor}`:` (`1.5X higher` or `1.5X lower`) selected).

Based on these fits, we estimate that at maximum excitation power, our $\theta = 0$ excitation rate is slightly higher than excited state decay $(h_{exc}\sigma_{01} \approx 1.9(1/\tau_{exc})$, corresponding to $\overline{n_2} \approx 0.32)$. Maximum stimulation power depletes ~8% of this fluorescence, corresponding to a $\theta = 0$ stimulation rate slightly lower than excited state decay $(h_{stim}\sigma_{23} \approx 0.32(1/\tau_{exc}))$. This confirms our expectation that the stimulation intensity we used in Figures 3 and 4 yields an appreciable level of fluorescence depletion.

Orange bead excitation and emission rates

In order to quantify the rates of excitation and stimulation, we imaged index-matched orange bead fluorescence as illustrated in Figure 2b with `Imaging method: Fluorescence depletion imaging` and `Fluorescent sample type: Beads labeled with orange dye` selected. Figure 5 in the main article with `Fluorescent sample type: Beads labeled with orange dye` selected shows the results as we illuminated the orange beads with variable-power excitation pulses up to 1/8 the maximum power used for crimson beads, and full-power stimulation pulses. The camera exposure parameters were identical to those for the crimson bead in Figure 5. Based upon the lower stimulated emission cross-section of the orange beads with respect to crimson beads, the model in Figure 1c predicted reduced orange fluorescent depletion. We indeed observed no depletion above the noise threshold of our detector.

Our orange fluorescence measurements are consistent with our previously described model for the excited state population fraction $\overline{n_2}$ (Figure 5 with `Fit parameter` R_{fluor}`: Subjectively optimal` and `Fluorescent sample type: Bead labeled with orange dye` selected). Using $R_{fluor} = 7.04 \times 10^{-3}$ counts^{-1}, $R_{exc} = 27.0$ W^{-1}, and $R_{stim} = 0.2$ W^{-1} gives model predictions (green and red lines) that strongly resemble our experimental data (green and red dots). Neighboring values also produce reasonable fits. The green shaded area shows the range of the $P_{stim} = 0$ model (green line) as we vary R_{exc} by ± 7%. The red shaded area shows the range of the $P_{stim} \neq 0$ model (red line) as we vary R_{stim} by ± 40%. Grossly different values of R_{fluor} fit the data poorly for any value of R_{exc} and R_{stim} (Figure 5 with `Fit parameter` R_{fluor}`:` (`1.5X higher` or `1.5X lower`) selected).

Based on these fits, we estimate that at the maximum excitation power we used for the orange beads, our $\theta = 0$ excitation rate is higher than excited state decay $(h_{exc}\sigma_{01} \approx 3.5(1/\tau_{exc})$, corresponding to $\overline{n_2} \approx 0.42)$. The orange bead fluorescence appears

more saturated than the crimson bead fluorescence when both are driven with the same thermal load; this may be attributed to the higher Φ of the orange beads. If the orange beads had a lower number of fluorophores per bead than the crimson beads, this would also contribute to greater saturation of orange fluorescence. Maximum stimulation power depletes a negligible amount of this fluorescence, corresponding to a $\theta = 0$ stimulation rate more than an order of magnitude lower than excited state decay $(h_{stim}\sigma_{23} \approx 0.046(1/\tau_{exc}))$.

Dark-field imaging of stimulated emission

While our experimental results using fluorescent beads appear to fulfill the expectations of our model for stimulated emission, this model is not fluorophore-specific. We expect that switching to a different type of fluorophore—nanodiamonds doped with fluorescent nitrogen vacancy centers—should yield similar results, and should allow us to test several other expectations.

Although the model in Figure 1c does not include elastic scattering from the fluorescent particle, we expect stimulated emission and scattered light—which are both coherent with the stimulation beam—to coherently interfere with one another. Fluorescent nanodiamonds are highly scattering particles (due to their high refractive index) and are therefore a useful sample type to test this expectation.

Fluorescent nanodiamonds don't photobleach, which allows for unlimited images of the same particle. Acquiring images of the sample at many axial positions is useful for testing the expectations that stimulated emission images should defocus like scattered light images. Acquiring images of the sample with many different excitation and stimulation powers allows us to test the expectation that stimulated emission should increase with increasing excitation and stimulation power. We expect this because the stimulated emission rate depends on both stimulation intensity h_{stim} and excitation fraction n_2 [Hell 1994], and because our nanodiamond fluorescence and depletion measurements (Figure 5 with `Fluorescent sample type: Nanodiamonds doped with N-v centers` selected) indicate that our lasers do not saturate either excitation or stimulation.

We used dark-field imaging to attempt to image stimulated emission from N-v centers in nanodiamonds (Figure 2b with `Imaging method: Dark-field imaging of stimulated emission and scattered light` and `Fluorescent sample type: Nanodiamonds doped with N-v centers` selected). This experiment mimics one version of our thought experiment in Figure 1 (Figure 1a, 1b, or 1c with `Imaging method: Dark-field` selected). We chose dark-field imaging, as opposed to phase contrast imaging, because the coherent background from phase contrast imaging could complicate any interference between the extremely bright scattered light and stimulated emission.

We imaged the nanodiamonds by taking five exposures with different excitation pulse delays, yielding dark-field images of nanodiamonds 2.5 µs before excitation, 1.25 µs before excitation, during excitation, 1.25 µs after excitation, and 2.5 µs after excitation. For each exposure, we used 24 full-intensity excitation/stimulation pulse pairs with 1.25 µs pulse duration and 600 µs between consecutive pairs. We expect efficient and highly selective excitation/stimulation; 532 nm is near the N-v excitation peak but far from the emission peak, and vice versa for 721 nm (Figure 2b, upper right panel, with `Fluorescent sample type: Nanodiamonds doped with N-v centers`).

The left panel of Figure A3 (Figure A3a with `z position: 0.0 µm` selected) shows a 200-exposure average of dark-field images of an in-focus nanodiamond 2.5 µs before excitation. As with the crimson beads, we expect no stimulated emission at this delay because the stimulation and excitation pulses don't overlap in time, and the pulse pair repetition time (600 µs) is orders of magnitude larger than the N-v center excited state lifetime τ_{exc} (~12 ns). The "difference image" in the right panel of Figure A3 shows the the change in the corresponding left panel image when the excitation and stimulation pulses overlap in time, compared to when they don't.

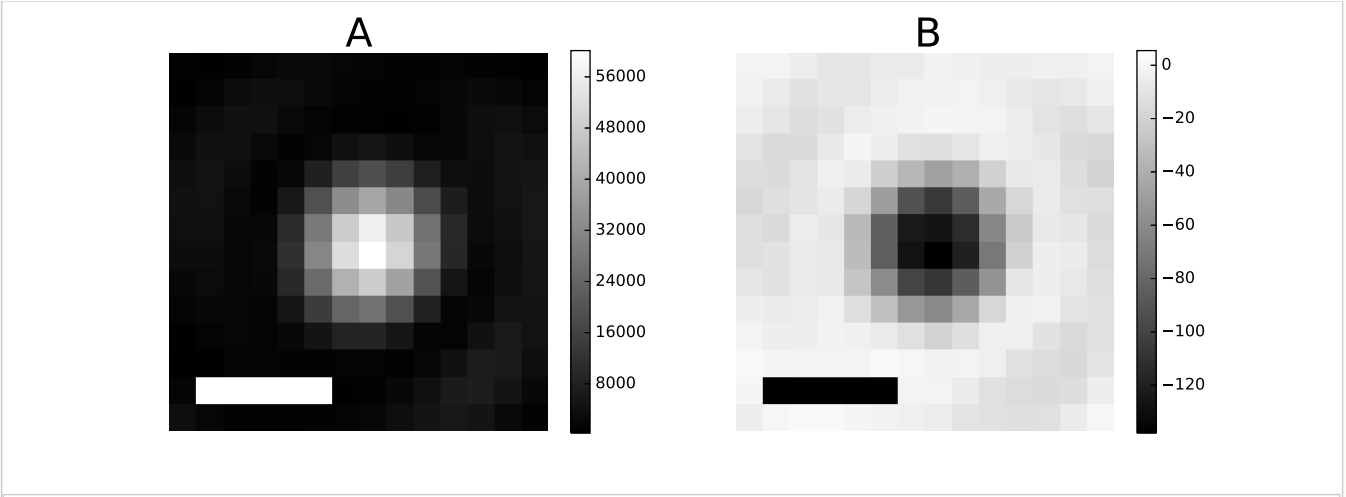

Figure A3: The change in scattered light from nanodiamonds due to excitation. (A) Dark-field image of a nanodiamond due to scattered light from the stimulation beam alone. **(B)** The change in (A) due to simultaneous excitation and stimulation beams. Use the `Z position` control above to change the Z focus of the images in steps of 200 nm (X and Y are the horizontal and vertical axes, respectively). Click here for XZ and YZ views of the images. Scale bar: 250 nm. See the Appendix for details of image acquisition, image processing, and figure generation.

The difference image in Figure A3b clearly depicts the nanodiamond. If this difference image is due to stimulated emission, it contradicts the model in Figure 1b (which predicts that stimulated emission cannot convey information about the location of the emitter) and supports the model in Figure 1c, which predicts a point-like stimulated emission image for any point-like fluorescent particle. Interference between stimulated emission and scattering can explain the scattered light image of the nanodiamond appearing to dim due to excitation (click here for an estimation of the relative phase between stimulated emission and nanodiamond scattering).

The model in Figure 1c also predicts that stimulated emission from a point-like fluorescent particle should defocus identically to scattering from the particle. To test this prediction, we moved the nanodiamond in Figure A3 to fourteen different axial positions outside the focus of the imaging system and acquired scattered light and difference images (Figure A3 with `Z position: -1.2 µm to 1.6 µm`). We found that the difference image defocused very similarly to the scattered light image (as well as the fluorescence image), which is consistent with our model.

If the dark-field difference images in Figure A3 are due to stimulated emission from the nanodiamonds, we expect that the magnitude of the difference image signal should increase with increasing excitation and stimulation power. Using the same image acquisition and averaging parameters as we did for Figure A3, while varying the excitation and stimulation power, we found that the magnitude of the difference image signal from the nanodiamond increased with increasing excitation and stimulation.

Nanodiamond excitation and emission rates

In order to quantify the rates of excitation and stimulation, we imaged nanodiamond fluorescence as illustrated in Figure 2b with `Imaging method: Fluorescence depletion imaging` and `Fluorescent sample type: Nanodiamonds doped witn N-v centers` selected. Figure 5 in the main article with `Fluorescent sample type: Nanodiamonds doped witn N-v centers` selected shows the results as we illuminated the nanodiamonds with variable-power excitation pulses and full-power stimulation pulses. As with the nanodiamond in Figure A3, at each excitation power, we took five exposures with different stimulation pulse delays, yielding fluorescence images of a nanodiamond excited 2.5 µs before stimulation, 1.25 µs before stimulation, during stimulation, 1.25 µs after stimulation, and 2.5 µs after stimulation. For each exposure, we used 700 excitation/stimulation pulse pairs with 1.25 µs pulse duration and 600 µs between consecutive pairs. As with the crimson dye, the emission spectrum of the nanodiamonds (inset in Figure 2b with `Fluorescent sample type: Nanodiamonds doped with N-v centers` selected) nicely overlaps with the stimulation wavelength, so we expect depletion when the stimulation and excitation lasers coincide on the sample. Indeed, this is what we observe in Figure 5. An axial view of the nanodiamond fluorescence and depletion at maximum excitation and stimulation power is also available.

Our nanodiamond fluorescence measurements are fairly consistent with our previously described model for the excited state population fraction $\overline{n_2}$ (Figure 5 with `Fit parameter` R_{fluor}`: Subjectively optimal` and `Fluorescent sample type: Nanodiamond doped witn N-v centers` selected). Using $R_{fluor} = 4.35 \times 10^{-3}$ counts^{-1}, $R_{exc} = 1.98$ W^{-1}, and $R_{stim} = 02.08$ W^{-1} gives model predictions (green and red lines) that reasonably resemble our experimental data (green and red dots). Neighboring values also produce reasonable fits. The green shaded area shows the range of the $P_{stim} = 0$ model (green line) as we vary R_{exc} by ± 7%. The red shaded area shows the range of the $P_{stim} \neq 0$ model (red line) as we vary R_{stim} by ± 40%. Grossly different values of R_{fluor} fit the data poorly for any value of R_{exc} and R_{stim} (Figure 5 with `Fit parameter` R_{fluor}`:` (`1.5X higher` or `1.5X lower`) selected).

The fit to experimental data is not as close as the fit for the crimson and orange bead fluorescence. Others have measured a similar N-v fluorescence saturation shape [Geiselmann 2013], and additionally, N-v centers have only four distinct alignment angles for single crystal diamonds (N.B. it's not clear whether we are imaging single or multiple crystals). However, the model for isotropically aligned fluorophores appears to give a reasonable qualititative fit.

Based on these fits, we estimate that at maximum excitation power, our $\theta = 0$ excitation rate is slightly higher than excited state decay $(h_{exc}\sigma_{01} \approx 2.9(1/\tau_{exc})$, corresponding to $\overline{n_2} \approx 0.39)$. Maximum stimulation power depletes ~10% of this fluorescence, corresponding to a $\theta = 0$ stimulation rate slightly lower than excited state decay $(h_{stim}\sigma_{23} \approx 0.62(1/\tau_{exc}))$. This confirms our expectation that the stimulation intensity we used in Figure A3 yields an appreciable level of fluorescence depletion in our nanodiamonds.

Axial view of fluorescence from a nanodiamond doped with N-v centers

The fluorescence plot in Figure 5 (inset) in the main text shows transverse in-focus views of the fluorescence from crimson and orange beads, as well as from a nanodiamond doped with N-v centers. These are XY views, where X and Y refer to the horizontal and vertical axes, respectively. Figure A4 below shows an XZ view (averaged over the Y axis) of a stack of fluorescence images taken with varying axial position of the nanodiamond relative to focus. Also shown is the XZ view of the change in fluorescence due to stimulated emission depletion. The images used to generate the image stack were taken in 200 nm axial steps. There were 700 excitation/stimulation pulse pairs during each exposure, with 600 µs between each pair. Each Z slice in the figure is generated by averaging 20 such exposures at a single axial position and then simply averaging over the vertical dimension. We were able to generate such a projection due to the absence of photobleaching in N-v centers. Collecting the required number of fluorescence images from crimson or orange beads to make a similar axial projection is complicated by photobleaching of those dyes.

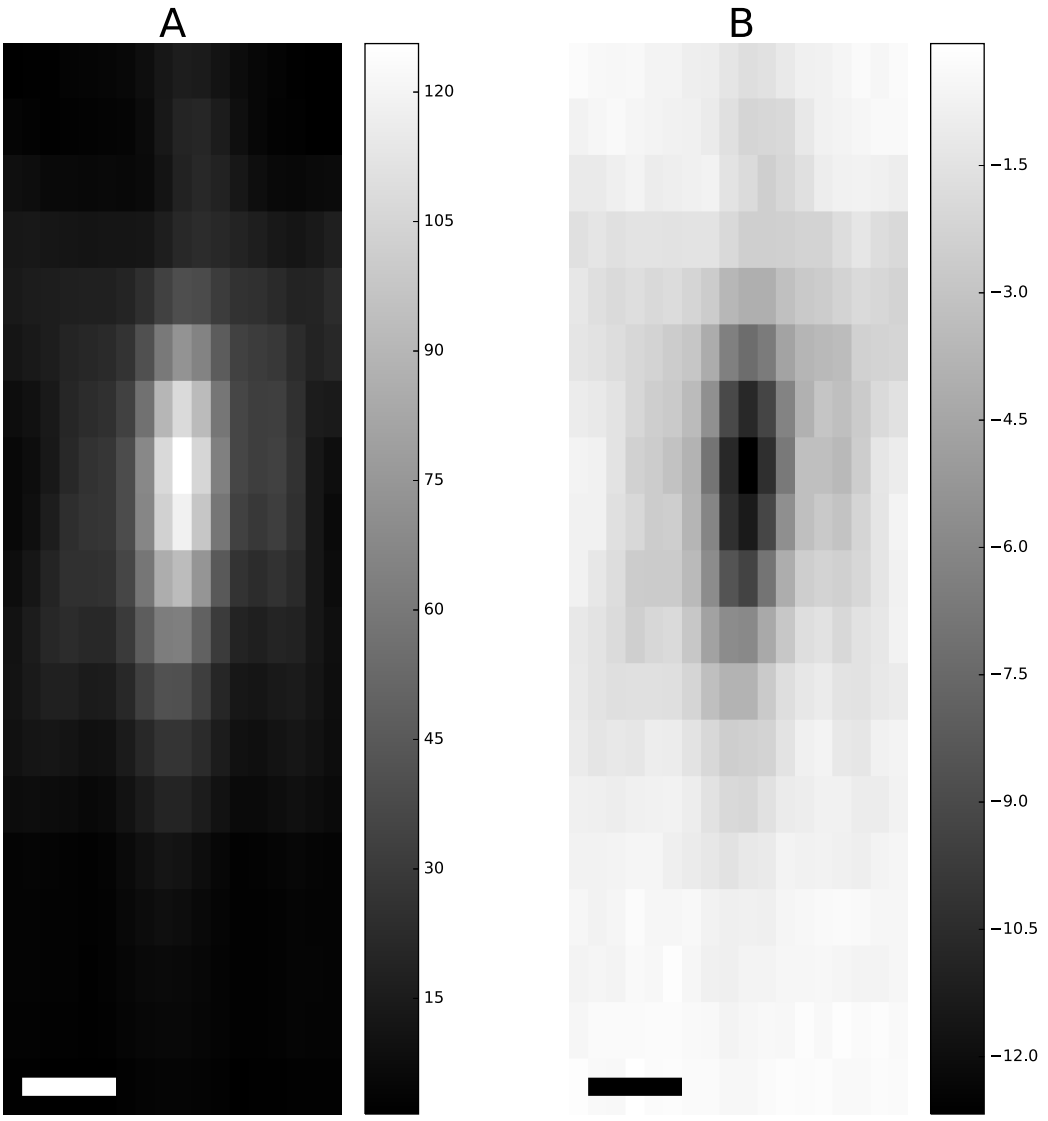

Figure A4: XZ view of fluorescence from a nanodiamond doped with N-v centers. (A) XZ image of fluorescence. (B) XZ image of depletion of fluorescence due to stimulated emission. Adjacent rows in these images are 200 nm apart in the axial direction. Scale bar: 350 nm.

Dark-field image generation

Dark field image acqusition details

We perform dark-field imaging of excited fluorescent nanodiamonds in a setup outlined in the main article (Figure 2b with `Imaging method: Dark-field imaging of stimulated emission and scattered light` and `Fluorescent sample type: Nanodiamonds doped with N-v centers` selected). We illuminate the nanodiamonds with a train of several green excitation (532 nm) laser pulses as well as several pulses of red (721 nm) laser light in order to stimulate emission from the samples. We place a chrome disc in a back focal plane of the imaging path in order to block the transmitted stimulation light and allow the scattered light and stimulated emission to reach the camera. The excitation and stimulation laser pulses are always the same duration as each other, and they are typically 1.25 µs (our shortest available duration). The excitation and stimulation trains have 600 µs between pulses of the same color. Our experiments involve five sequential camera exposures:

1. During the first exposure, the red pulse train precedes the green pulse train by 2.5 μs. Because 600 μs is much longer than the excitation lifetime, there should be no stimulated emission.
2. During the second exposure, the red pulse train precedes the green pulse train by 1.25 μs. The falling tails of the red pulses very slightly overlap with the rising edges of the green pulses, so a small amount of stimulated emission may be possible.
3. During the third exposure, the red and green pulses are simultaneous. Stimulated emission should be possible.
4. During the fourth exposure, the red pulse train follows the green pulse train by 1.25 μs. The rising edges of the red pulses very slightly overlap with the falling tails of the green pulses, so a small amount of stimulated emission may be possible.
5. During the fifth exposure, the green pulse train precedes the red pulse train by 2.5 μs. Because 2.5 μs is much longer than the excitation lifetime, there should be no stimulated emission. If the green pulse modifies the sample in a time-delayed fashion (e.g. heating) and this effect persists longer than 2.5 μs, there may be some effect on the dark-field image.

We additionally take a second five-exposure sequence with the green beam blocked. This a control for "crosstalk", a small effect of the green AOM operation on the red AOM transmission.

Dark field and difference image processing

The difference between the first and third exposure (of the five listed above) should let us know the effect of excitation on the phase contrast image of the beam. However, the stimulation laser intensity fluctuations are larger than the change due to excitation, so we typically take hundreds of five-exposure sequences and average the result to improve our sensitivity, and we also use the 4000-count coherent background to estimate stimulation laser brightness and re-scale the image. Because the sample moves over the time required to acquire all of the exposures, we employ image registration prior to averaging. This is the image processing sequence that returns scattered light images that allow us to observe changes due to excitation (example code):

1. We estimate the average brightness of the red laser by averaging all dark-field images and then finding the mean pixel value of the regions of the image that do not contain the nanodiamond (the background).
2. We estimate the brightness of the red laser in each exposure by finding the mean pixel value of the background of each exposure.
3. We re-scale individual exposures by a factor of the ratio of the average background to the individual exposure background.
4. We choose a nanodiamond image as the registration reference, and then register each scattered light image to the reference. Doing this well involves careful tuning of registration parameters.
5. We average the scattered light images for each of the five excitation/stimulation delays.
6. We compute "difference images": the difference between a particular scattered light image and the scattered light image when the stimulation pulse precedes excitation. We compute a second set of difference images in the case of the blocked green light, and subtract the "green blocked" from "green on" difference images to get the crosstalk-corrected difference image that accurately shows the change in scattering due to excitation.

While we use 750x total magnification (8.7 nm/pixel) to give large dynamic range, this is not great for viewing our difference images, because intra-pixel fluctuations can appear to swamp the signal. Prior to displaying the scattered light and difference images of the nanodiamonds, we bin 8 x 8 regions of pixels to give a more typical size (69.6 nm/pixel).

Figure A5 below shows a sample scattered light image of a nanodiamond prior to excitation, and the change in that image before, during and after excitation, based on the experimental method and image processing steps delineated above. For each exposure, we used 25 maximum-intensity excitation/stimulation pulse pairs, and the images are a 200-exposure average.

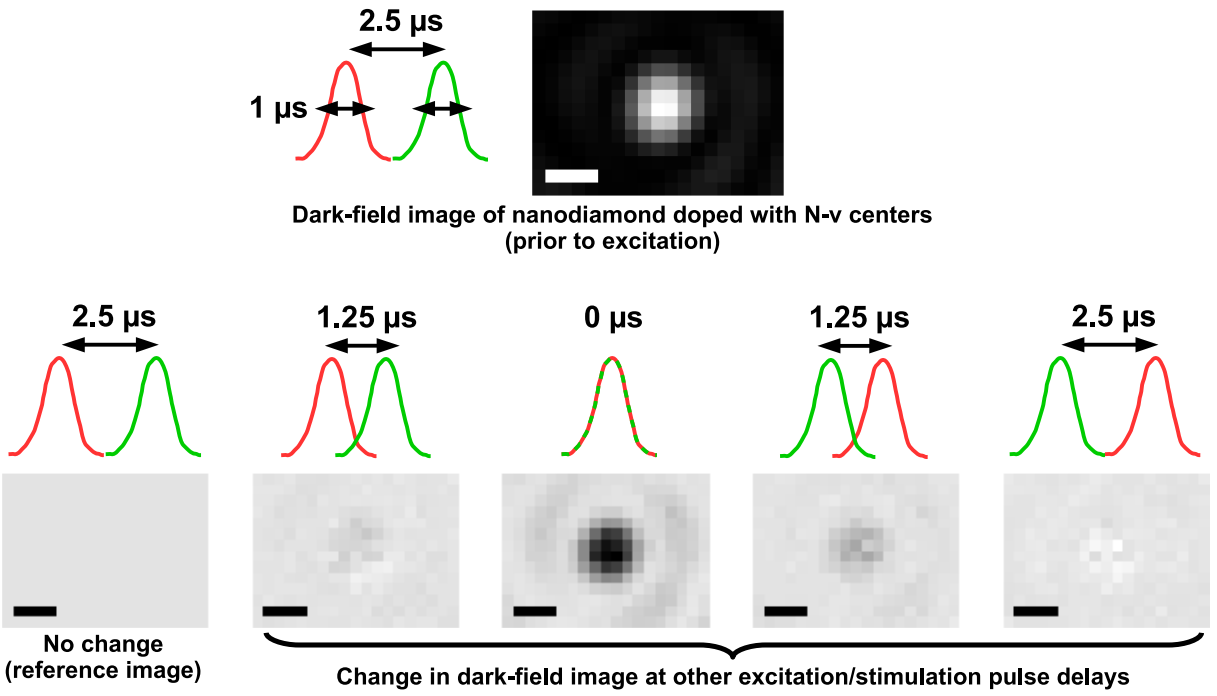

Figure A5: The change in the dark-field nanodiamond image due to excitation has a sub-microsecond response time. Scanning the delay between the excitation (green) and stimulation (red) laser pulses shows the observed change in the scattered red light signal has a timescale at least as short as the laser pulse duration (1.25 µs). Scale bar: 280 nm.

Axial view of the change in scattered light from a nanodiamond due to excitation

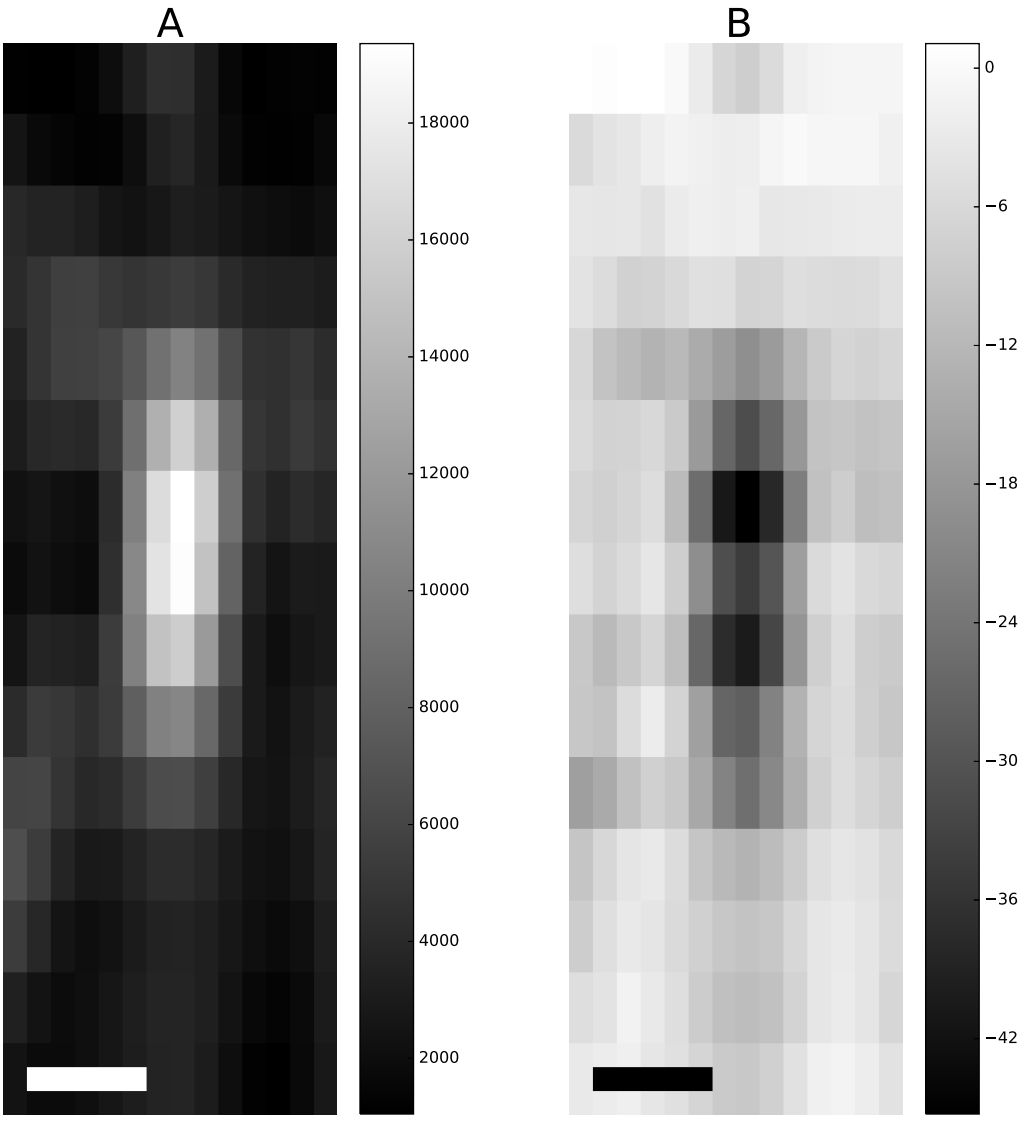

Axial view: XZ ▾ (change this to adjust the axial view of the image)

Figure A6: Axial view of the change in scattered light from a nanodiamond due to excitation. (A) Dark-field image of a nanodiamond due to scattered light from the stimulation beam alone. **(B)** The change in (A) due to simultaneous excitation and stimulation beams. Use the `Axial view` control above to switch between XZ and YZ views, or click here for transverse (XY) slices of the images at various axial (Z) sample positions. Adjacent rows in these images are 200 nm apart in the axial direction. Scale bar: 350 nm. Follow these links for details of image acquisition, image processing, and figure generation.

Estimating the phase between stimulated emission and scattering

The results in Figure A3 suggest that stimulated emission from a nanodiamond makes the scattered light image darker. This could happen if the scattered electric field destructively interferes with the stimulated emission electric field. Interference is possible because both stimulated emission and scattered light are coherent with the incident electric field, and therefore have a distinct phase relationship with each other.

To predict this phase relationship, we start with incident electric field $E_0 e^{i\omega t+\phi_0}$, stimulated emission field $E_{stim} e^{i\omega t+\phi_{stim}}$, and scattered field $E_{scat} e^{i\omega t+\phi_{scat}}$. Because stimulated emission is considered a nearly instantaneous process [Townes 1964], there is no delay between the incident electric field and the stimulated emission electric field:

$$\phi_{stim} = \phi_0$$

We also know elastically scattered light has a minimum $\frac{\pi}{2}$ phase delay with respect to the incident electric field [Zernike 1955], and larger delay for light scattered by particles that do not have a sufficiently small diameter for the Rayleigh approximation $d \ll \frac{\lambda}{\pi}$, so:

$$\phi_{scat} - \phi_0 \geq \frac{\pi}{2}$$

Our diameter $d \approx 80$ nm nanodiamonds are slightly larger than the small diameter approximation allows for $\lambda = 721$ nm. To estimate the additional refractive phase shift, we note that the refractive index of diamond $n_{diamond} = 2.42$, while the mounting medium $n_{oil} = 1.52$, with a difference $\Delta n_{refractive} = 0.9$. The approximate phase difference due to different refractive optical path lengths is:

$$\Delta\phi_{refractive} \approx \frac{2\pi d \Delta n_{refractive}}{\lambda} \approx 0.6$$

We can then estimate the relative phase between scattered light and stimulated emission:

$$\Delta\phi = \phi_{scat} - \phi_{stim} \approx \frac{\pi}{2} + \Delta\phi_{refractive} \approx 2.2$$

This fulfills the requirement for destructive interference:

$$\frac{\pi}{2} < \Delta\phi < \frac{3\pi}{2}$$

The difference image signal depends on excitation and stimulation power

We expect stimulated emission in our samples to increase with both excitation and stimulation power. This is because the stimulated emission rate should depend on both stimulation intensity h_{stim} and excitation fraction n_2, and because we did not fully saturate excitation or stimulation in any of our samples.

To test this expectation, we imaged the nanodiamond from Figure A3 with increasing excitation and stimulation power while keeping the laser pulse length, as well as all other imaging and acquisition parameters the same. Figure A7 shows the change in brightness of the main scattered lobe from the nanodiamond (spatially averaged over a 500 nm square) as it varies by increasing excitation and stimulation beam peak power. As predicted, the signal magnitude increased with increasing excitation and stimulation power.

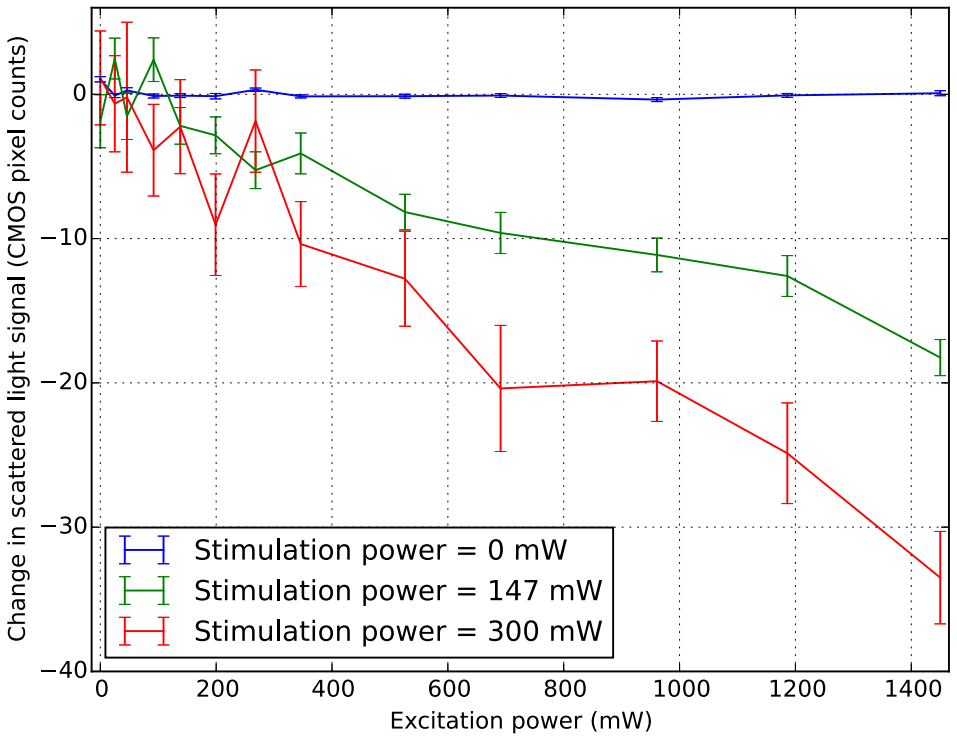

Select data: All excitation powers

Figure A7: The change in nanodiamond scattering when excitation and stimulation power is varied. The dark-field scattered light image of a nanodiamond doped with N-v centers becomes dimmer when in the presence of the excitation beam, and the magnitude of the brightness change increases for increasing excitation and stimulation beam power. Each data point reflects a 200-repetition average of the change in brightness of the main scattered lobe of the diamond (spatially averaged over a 500 nm square). Use the `Select data` control to view all or selected excitation and stimulation powers. Follow these links for details of image acquisition, image processing, and figure generation.

Another way to confirm that the change in scattered light signal depends on both excitation and stimulation intensity is to use longer laser pulses while keeping the pulse energy constant. In the unsaturated regime, both excitation and stimulation rates are intensity-dependent, whereas total fluorescence is fluence-dependent. Figure A8 below shows the change in scattering of a nanodiamond due to simultaneous excitation and stimulation pulses of 5 μs, 3.75 μs, 2.5 μs and 1.25 μs with the intensity tuned so that the total energy per pulse (and average power) is the same for all pulse lengths. Each scattered light image was taken using 30 excitation/stimulation pulse pairs per exposure, and the difference images shown are generated by subtracting a 200 exposure average of images taken without simultaneous excitation/stimulation from images with simultaneous excitation/stimulation.

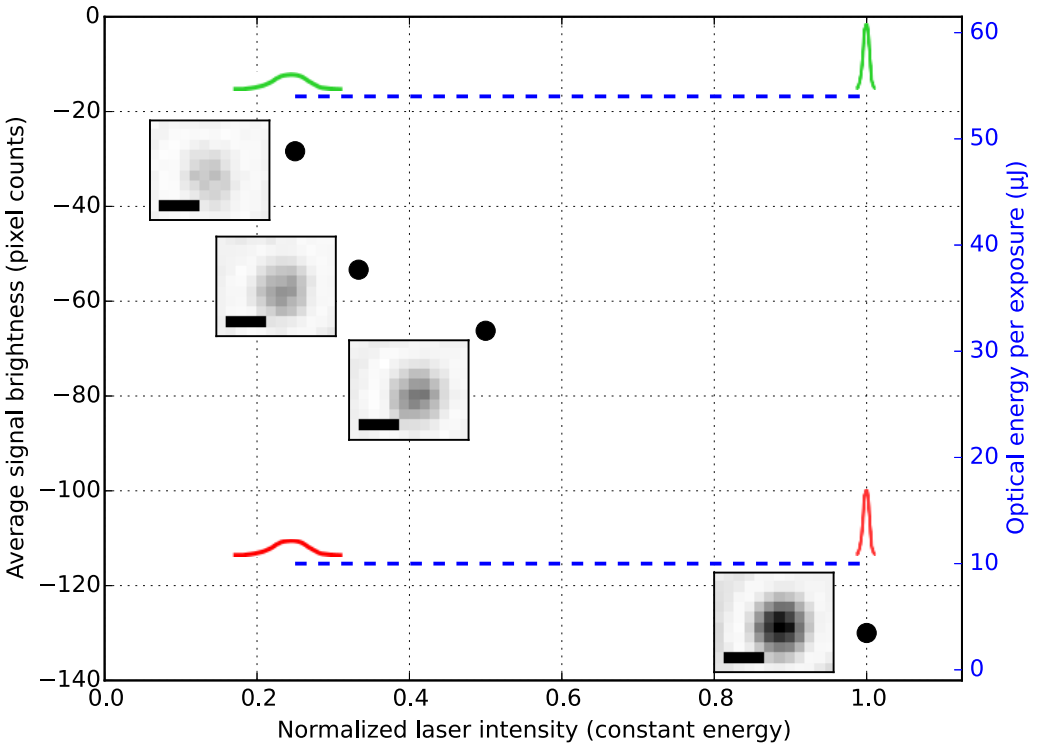

: Dark-field difference images of excited fluorescent nanodiamonds with varying peak excitation/stimulation intensity. A N-v center doped nanodiamond is irradiated by simultaneous excitation and stimulation pulses of 5 μs, 3.75 μs, 2.5 μs, and 1.25 μs duration with energy per pulse kept constant. Each point on the graph is the average change in brightness per pixel in a 173 nm square region centered at the main scattered lobe of a 200-exposure average of dark-field images. Inset images correspond to the nearest data point. Scale bar: 280 nm. Follow these links for details of image acquisition, image processing, and figure generation.

The difference image signal monotonically increases with increasing laser intensity, even though the delivered energy is the same for all pulse lengths. This behavior, which is starkly unlike fluorescence, is not unique to stimulated emission; photothermal imaging is also intensity-dependent. Regardless, we similarly performed phase contrast imaging of four index-matched crimson beads using excitation/stimulation pulse pairs with 10 μs, 5 μs, 2.5 μs, and 1.25 μs duration (we used a different bead for each pulse length to avoid photobleaching effects). Each phase contrast image was taken with eight excitation/stimulation pulse pairs per exposure with a phase plate angle set to maximize the contrast of the difference images. The difference images are generated by subtracting 50-exposure averages of the phase contrast images without simultaneous excitation/excitation from images with simultaneous excitation/stimulation. We found that, as with the nanodiamond, the crimson bead difference image signal magnitude increased monotonically for increasing excitation and stimulation intensity (see results in Figure A9 below).

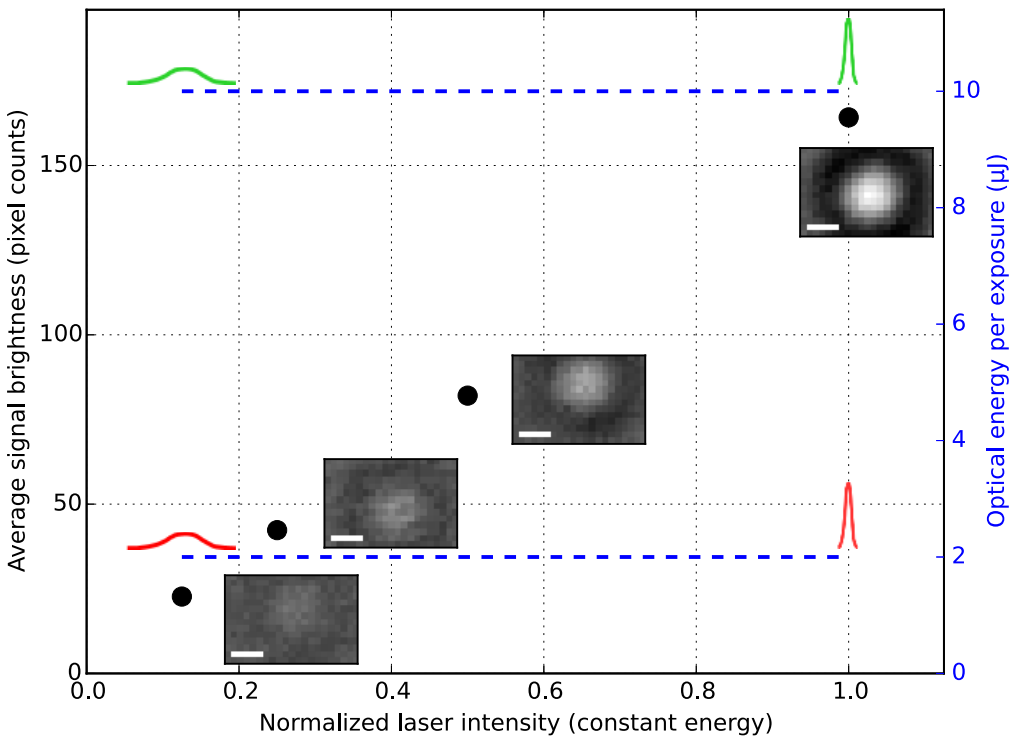

Figure A9: **Phase contrast difference images of excited crimson beads with varying peak excitation/stimulation intensity.** Crimson fluorescent polystyrene beads are irradiated by simultaneous excitation and stimulation pulses of 10 μs, 5 μs, 2.5 μs, and 1.25 μs duration with energy per pulse kept constant. Each point on the graph is the average change in brightness per pixel in a 208 nm square region centered at the main lobe of a 50-exposure average of phase contrast difference images. Inset images correspond to the nearest data point. Scale bar: 350 nm. Follow these links for details of image acquisition, image processing, and figure generation.

Phase contrast imaging of an excited fluorescent nanodiamond

Earlier in the appendix, we showed how we used dark-field imaging, and not phase contrast imaging, to attempt to image stimulated emission from fluorescent nanodiamonds. These nanodiamonds are not an ideal candidate for phase contrast imaging of stimulated emission. Their extremely high refractive index (2.42) prevents index-matching and yields bright, coherent scattering. Given our experimental parameters, the stimulating light that is scattered by a nanodiamond can fill the dynamic range of our camera in less than 40 μs. The power of the elastically scattered light dominates that of the nanodiamond fluorescence by a factor of ~6,000:1. Given the ~10% depletion measured, we extrapolate that the scattered light intensity would dominate stimulated emission intensity by ~60,000:1. While phase contrast imaging could boost stimulated emission signal by interference with a coherent background, the scattered light is also coherent, and the magnitude of the interference term between the transmitted light background and the scattered light would still dominate that between transmitted light and stimulated emission. As such, we expect that, even with phase contrast imaging, any stimulated emission from the nanodiamonds would be visible only as a small perturbation of the scattered light signal (similar to our dark-field results). Regardless, we performed phase contrast imaging of excited nanodiamonds (Figure 2b in the main article with `Imaging method: Phase contrast imaging of stimulated emission and scattered light` and `Fluorescent sample type: Nanodiamonds doped with N-v centers` selected) to confirm this expectation.

In this experiment, we took advantage of the fact that our nanodiamonds do not bleach and took many phase contrast images of our nanodiamond samples with a fine scan of phase plate angles. The 32 phase plate angles were separated in steps of 0.2°, over a total range of 6.2°. The angle of the phase plate maps nonlinearly onto the relative phase angle between transmitted light and scattered light, resulting in an average optical phase shift of ~14° for each phase plate step. At each phase plate angle, we took five exposures with different relative delays between excitation and stimulation pulses: $\Delta\tau$ = -2.5 μs, -1.25 μs, 0 μs, 1.25 μs, and 2.5 μs. We repeated this sequence 1000 times for each phase plate angle. During each exposure, two 1.25 μs duration excitation and stimulation pulse pairs were incident on the camera with 600 μs delay between each pair. In between exposures, a constant stream of 1.25 μs excitation pulses illuminated the camera with 600 μs inter-pulse spacing in order to maintain thermal stability of the

sample, though we did not detect any sample heating artifacts using these laser exposure parameters. Figure A10 below shows the results of this experiment.

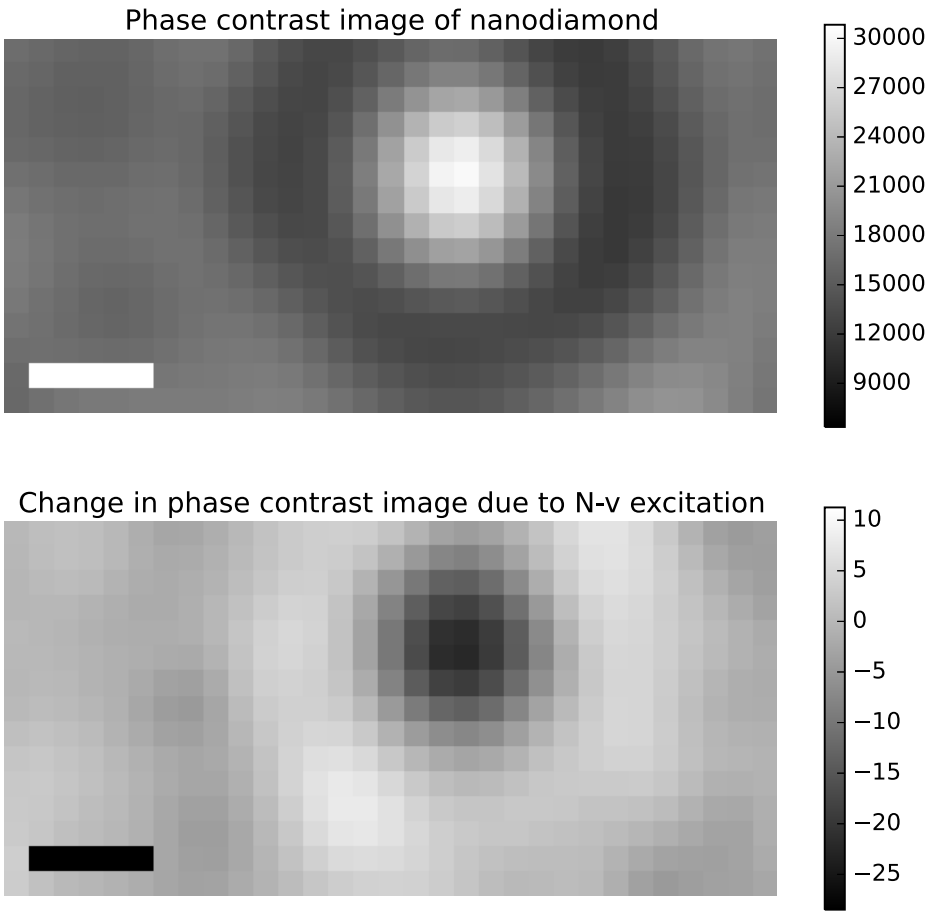

Phase plate position #: 0 (Adjust the phase of the transmitted light relative to scattered light)

Figure A10: The change in the phase contrast image of a fluorescent nanodiamond due to excitation. Upper panel: phase contrast image of a nanodiamond that is not excited. Lower panel: the difference in the opper panel due to excitation. Use the `Phase plate position #` control to choose a phase plate angle in order to tune the relative phase between transmitted and scattered light. Adjacent phase plate positions correspond to roughly 14° phase shift. Color bars: image intensity (camera digitizer units). Scale bar: 350 nm. Follow these links for details of image acquisition, image processing, and figure generation.

A phase contrast image of light scattered from a nanodiamond is in the upper panel of Figure A10. This image is an average of the nearly 1000 exposures taken when the stimulation laser pulse preceded the excitation pulse by 2.5 μs at a single phase plate angle ("nearly 1000" because we ignored exposures during which a dust particle entered the emission beam path). The lower panel of Figure A10 shows a difference image: the difference between the 1000 exposure average of the phase contrast image with simultaneous stimulation and excitation pulses versus the corresponding image in the above panel. By adjusting the phase plate angle (Figure A10 with `Phase plate position #: 0-31` selected) we observe that the maximum negative contrast of the difference image corresponds with the maximum positive contrast image of the scattered light, and vice versa. As with the darkfield measurement, the phase contrast difference image appears to resemble a decrease in the magnitude of scattered light due to coincident excitation and stimulation. The phase contrast technique did not appear to provide further information about stimulated emission from fluorescent nanodiamonds.

How we made the animations

Each frame of one of our animations is a slide in a LibreOffice Impress presentation. We created the content of each frame by using geometric shapes available within the program. After we finished drawing all of the frames, we saved the presentation in an HTML format (available using `File > Save As`). This action generates an individual `.png` file for each frame (ancillary files are also generated; these may be ignored or deleted). We then ran a python script that uses FFmpeg (which must be installed prior) to generate an `.mp4` video out of all of the `.png` files. The Impress presentations and python scripts are found in the figure generation folder.

How we made the experimental setup figure

We took the photograph in Figure 2a with a smartphone camera, and then cropped and saved it in `.png` format. We then annotated it with numbers in LibreOffice Impress, and then saved the `.odp` file in `.pdf` format (available using `File > Export as pdf`). We finally converted the `.pdf` to `.svg` format using pdf2svg (place in pdf2svg distribution folder and then use command prompt call: `pdf2svg *.pdf *.svg`).

For Figure 2b, we drafted the bare-bones experimental setup in a LibreOffice Impress slide and then used that slide as a template for each particular iteration of the setup. We saved the `.odp` file to `.pdf` format as described above, and, we used an online tool to split the `.pdf` into separate `.pdf`s (example here). Finally, we converted each `.pdf` to `.svg` format using pdf2svg as described above.

The photograph, Impress presentation and pdf2svg distribution are found in the Figure 2 subfolder of the figure generation folder.

References

1. [Hell 1994] Hell, Stefan W., and Jan Wichmann. "Breaking the diffraction resolution limit by stimulated emission: stimulated-emission-depletion fluorescence microscopy." Optics letters 19, no. 11 (1994): 780-782. http://dx.doi.org/10.1364/OL.19.000780
2. [Berezin 2010] Berezin, Mikhail Y., and Samuel Achilefu. "Fluorescence lifetime measurements and biological imaging." Chemical reviews 110, no. 5 (2010): 2641-2684. http://dx.doi.org/10.1021/cr900343z
3. [Patterson 1997] Patterson, George H., Susan M. Knobel, Wallace D. Sharif, Steven R. Kain, and David W. Piston. ":Use of the green fluorescent protein and its mutants in quantitative fluorescence microscopy." Biophysical journal 73, no. 5 (1997): 2782-2790. https://doi.org/10.1016/S0006-3495(97)78307-3
4. [Johnson 2010] Johnson, Iain D. "Molecular Probes Handbook: A Guide to Fluorescent Probes and Labeling Technologies." Life Technologies Coroporation, 2010 https://www.thermofisher.com/us/en/home/references/molecular-probes-the-handbook.html
5. [Gruber 1997] Gruber, A., A. Dräbenstedt, C. Tietz, L. Fleury, J. Wrachtrup, and C. Von Borczyskowski. "Scanning confocal optical microscopy and magnetic resonance on single defect centers." Science 276, no. 5321 (1997): 2012-2014. http://dx.doi.org/10.1126/science.276.5321.2012
6. [Doherty 2013] Doherty, Marcus W., Neil B. Manson, Paul Delaney, Fedor Jelezko, Jörg Wrachtrup, and Lloyd CL Hollenberg. "The nitrogen-vacancy colour centre in diamond." Physics Reports 528, no. 1 (2013): 1-45. http://dx.doi.org/10.1016/j.physrep.2013.02.001
7. [Beveratos 2001] Beveratos, Alexios, Rosa Brouri, Thierry Gacoin, Jean-Philippe Poizat, and Philippe Grangier. "Nonclassical radiation from diamond nanocrystals." Physical Review A 64, no. 6 (2001): 061802. https://doi.org/10.1103/PhysRevA.64.061802
8. [Zondervan 2004] Zondervan, Rob, Florian Kulzer, Mikhail A. Kol'chenk, and Michel Orrit. "Photobleaching of rhodamine 6G in poly (vinyl alcohol) at the ensemble and single-molecule levels." The Journal of Physical Chemistry A 108, no. 10 (2004): 1657-1665. https://doi.org/10.1021/jp037222e
9. [Panchuk-Voloshina 1999] Panchuk-Voloshina, Nataliya, Rosaria P. Haugland, Janell Bishop-Stewart, Mahesh K. Bhalgat, Paul J. Millard, Fei Mao, Wai-Yee Leung, and Richard P. Haugland. "Alexa dyes, a series of new fluorescent dyes that yield exceptionally bright, photostable conjugates." Journal of Histochemistry & Cytochemistry 47, no. 9 (1999): 1179-1188. https://doi.org/10.1177%2F002215549904700910
10. [Casey 1988] Casey, Kelly G., and Edward L. Quitevis. "Effect of solvent polarity on nonradiative processes in xanthene dyes: Rhodamine B in normal alcohols." The Journal of Physical Chemistry 92, no. 23 (1988): 6590-6594.

http://dx.doi.org/10.1021/j100334a023

11. [Staudt 2007] Staudt, T. , Lang, M. C., Medda, R. , Engelhardt, J. and Hell, S. W. "2,2′-Thiodiethanol: A new water soluble mounting medium for high resolution optical microscopy." Microsc. Res. Tech., 70: 1-9. (2007) https://doi.org/10.1002/jemt.20396
12. [Jameson 2010] Jameson, David M., and Justin A. Ross. "Fluorescence polarization/anisotropy in diagnostics and imaging." Chemical reviews 110, no. 5 (2010): 2685-2708. http://dx.doi.org/10.1021/cr900267p
13. [Geiselmann 2013] Geiselmann, Michael, Renaud Marty, F. Javier García de Abajo, and Romain Quidant. "Fast optical modulation of the fluorescence from a single nitrogen-vacancy centre." Nature Physics 9, no. 12 (2013). http://dx.doi.org/10.1038/nphys2770
14. [Townes 1964] Charles H. Townes. "Nobel Lecture: Production of Coherent Radiation by Atoms and Molecules." (1964) Nobelprize.org. Nobel Media AB 2014. Web. 28 Nov 2017 https://www.nobelprize.org/nobel_prizes/physics/laureates/1964/townes-lecture.html
15. [Zernike 1955] Zernike, Frits. "How I discovered phase contrast." Science 121, no. 3141 (1955): 345-349. http://dx.doi.org/10.1126/science.121.3141.345